IOP Publishing Journal of Micromechanics and Microengineering
J. Micromech. Microeng. **32** (2022) 045006 (10pp) https://doi.org/10.1088/1361-6439/ac56ea

Solving curing-protocol-dependent shape errors in PDMS replication

Emilie Delplanque, Antoine Aymard, Davy Dalmas and Julien Scheibert*

Univ Lyon, Ecole Centrale de Lyon, ENISE, ENTPE, CNRS, Laboratoire de Tribologie et Dynamique des Systèmes LTDS, UMR 5513, F-69134 Ecully, France

E-mail: julien.scheibert@ec-lyon.fr

Received 20 July 2021, revised 2 February 2022
Accepted for publication 21 February 2022
Published 9 March 2022

Abstract

PolyDiMethylSiloxane (PDMS) is an elastomer increasingly used to produce soft objects by replication, in a variety of fields including soft electronics, microfluidics, tribology, biomechanics and soft robotics. While PDMS replication is usually considered faithful at all scales, down to nanoscales, detailed quantitative comparisons between the geometric features of the mold and the replicated object are still required to further ground this commonly accepted view. Here, we show that the top surface of centimetric parallelepipedic PDMS blocks, molded on a rigid plate, deviates from its expected flatness, the amplitude of the deviation being dependent on the crosslinking protocol. As a practical solution, we identify a suitable two-steps protocol which eliminates those replication errors. Using finite element simulations, we show that the effect originates from a thermal contraction when the sample cools from the curing temperature down to the operating temperature. This phenomenon actually applies at any length scale, and finely depends on the sample's aspect ratio and boundary conditions. Our results should help mitigating replication errors in all applications where a well-defined sample geometry is required.

Keywords: silicone rubber, Sylgard 184, shrinkage

(Some figures may appear in colour only in the online journal)

1. Introduction

PolyDiMethylSiloxane (PDMS) is a low cost elastomeric material combining large compliance, large toughness, good chemical resistance and biocompatibility. Sample preparation is relatively simple and usually involves crosslinking of the PDMS chains contained in a liquid mixture, inside a mold. In this respect, PDMS is usually deemed to enable good replication of the mold global shape and of the topographical features of its surfaces (roughness), down to the microscale, and even nanoscale [1–3]. And indeed, it has been used for replication purposes in a variety of fields including lab-on-chip [4], soft electronics [5], microfluidics [6, 7], biomechanics [8], soft robotics [9], metamaterials [10] and tribology [11–15].

The replication quality has been considered as an important question at small scales, micrometric and below [1]. In particular, it has been found that for the tiniest nanoscale features, the replication is more accurate when the crosslinked PDMS is stiffer and when, in its fluid state, it better wets the solid mold [2, 3, 16]. In contrast, the replication quality at large scales, millimeter or centimeter, has received relatively less attention. The issue is however crucial in some cases where a wide range of scales is of interest on the very same PDMS sample. As an example, Romero *et al* [17] considered a centimetric, nominally flat sample, decorated by an array of microspheres with individual heights intended to be controlled at the micrometer scale. Unexpectedly, when that sample was pressed against a flat glass plate, the pressure field was found

* Author to whom any correspondence should be addressed.

Table 1. Various single-step curing protocols for PDMS Sylgard 184 in the literature.

Temperature (°C)	Time (min)	References
150	10	[18, 19]
150	30	[20]
100	60	[21]
100	180	[22]
85	120	[23]
85	180	[21]
80	120	[24]
80	300	[25]
75	1440	[26]
70	30	[27]
70	2880	[11]
65	120	[28]
65	240	[21]
65	Overnight	[29, 30]
60	720 (12 h)	[31]
Room temperature	Overnight	[32, 33]
Room temperature	48 h	[33, 34]
Room temperature	9000 (6.25 days)	[12]

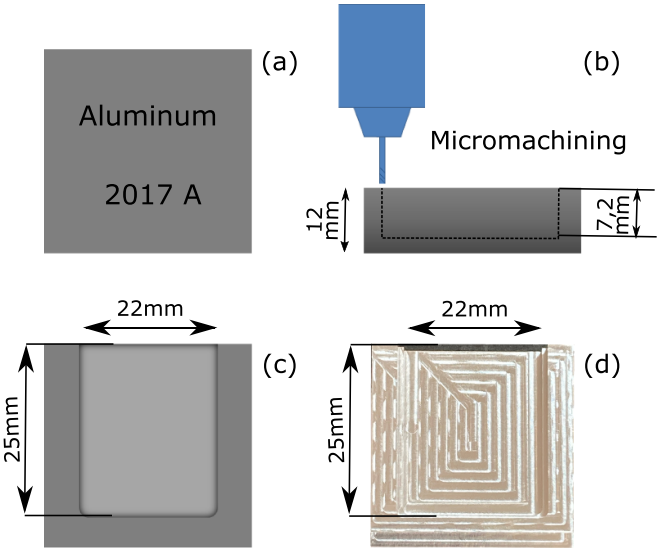

Figure 1. Mold preparation. A parallelepipedic block of Aluminum 2017A (a) is micro-machined to prepare a 7.2 mm deep cavity (b) of lateral sizes 22 mm × 25 mm (c). (d) Picture of the final mold.

heterogeneous at the overall sample scale. This observation suggested that the macroscopic shape of the sample departed from the expected flatness, by an amount sufficient to modify significantly the desired microspheres height distribution.

In this context, we revisit here the question of PDMS replication quality, with an experimental emphasis on large scales, by preparing parallelepipedic samples directly on rigid plates, and investigating the deviations to flatness of their largest free surface. For the material, we focus on the most widely used PDMS in the scientific literature: Dow Corning's Sylgard 184. In the vast majority of cases, it is crosslinked in a single step at a fixed temperature, before demolding. The curing temperature (from room temperature to 150 °C) and cross-linking duration (from a few minutes to several days) vary widely in the literature, as illustrated in table 1.

Here, by testing various curing protocols (section 2.1), we first show that no single-step protocol is capable of ensuring both a satisfactory replication quality (section 3.1) and a fully completed cross-linking reaction (section 3.2). We then propose a two-steps curing protocol which solves those two problems at once (section 4.1), and discuss the respective roles of the main aspects of this protocol (section 4.2). Finally, based on finite element calculations (section 3.4), we identify thermal contraction as the physical origin of the replication errors observed with single-step protocols (section 4.3), and discuss its dependence on sample size, aspect ratio and boundary conditions (section 4.4).

2. Methods

2.1. Sample preparation

The mold—A mold is fabricated out of an aluminum 2017 A block (30 mm × 30 mm ×12 mm). One face of the block is first prepared as a planar reference surface. Then, a 7.2 mm deep parallelepipedic cavity is excavated below that reference surface (see figure 1 for the dimensions), using a micro-milling machine (Minimill GX, Minitech) with a flat-ended tool of diameter 2 mm. The mold is then closed by pressing a lid made of a stack of three microscope glass slides (each of thickness 1 mm) on what remains of the reference plane, and held in place by two clips (red in figure 2). The stack of slides serves to increase the bending rigidity of the glass lid, thus avoiding any deviation from flatness of the final PDMS sample that would be simply due to a non-planar lid. Note that the milled cavity reaches one of the sides of the aluminum block (top side in figure 1(c)), thus enabling filling of the cavity with the fluid PDMS mixture from that side (see figure 2).

PDMS mixture—Sylgard 184 silicone elastomer is supplied as a two-parts liquid component kit: a pre-polymer base (part A) and a curing agent (part B). When mixed together, the obtained liquid is curable either at room temperature or at elevated temperatures ($T_{room} < T < 150$ °C) according to the Sylgard 184 Technical Data Sheet [35]. All PDMS samples fabricated are mixed at the recommended mass ratio of ten parts of base to one part of curing agent. To ensure standardization and repeatability across all samples, the mixing process is performed using a commercial mechanical stirrer (IKA Ministar 40). All samples are thoroughly mixed for a duration of 10 min at a speed of 500 rpm. In order to fabricate bubble free test samples, the mixed uncured PDMS is thoroughly degassed in a vacuum dessicator at low pressure for at least 30 min using a vacuum pump, until the mixture shows no more air bubbles. The very same degassed PDMS mixture is then poured into two containers, each enabling a specific measurement (see section 2.3): (i) the aluminum mold described in the previous paragraph (and closed with its glass lid) for topography

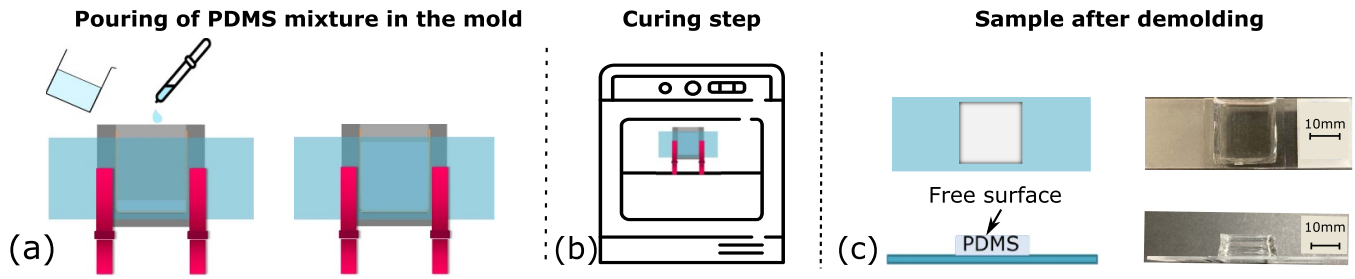

Figure 2. PDMS sample preparation. (a) The aluminum mold (grey part, same as in figure 1) is closed by a stack of three glass plates, and the liquid PDMS mixture is poured from top. After curing (b), the sample is carefully demolded, while remaining attached to one of the glass plates (c). The free surface on which profilometry measurements are performed is indicated on the bottom left sketch of (c). Right column of (c): pictures of a typical sample.

measurements and (ii) a Petri dish (diameter 54 mm) for elastic penetration depth measurements.

Curing protocols—The PDMS mixture is finally cross-linked, using one of the various following curing protocols, the outcomes of which will be compared in section *3*. First, we consider three single-step curing protocols, with three different combinations of temperature and curing time: (i) 48 h at 25 °C (as suggested in [35]), (ii) 5 h30 at 50 °C (two realizations) and (iii) 1 h30 at 80 °C (two realizations). At the end of the curing phase, the parallelepipedic PDMS sample is demolded by carefully removing the aluminum mold, which leaves the sample stuck on the first glass plate of the stack (see figure 2(c)). The exposed PDMS surface parallel to the glass plate, denoted from here and below as the 'free surface', is the one on which flatness measurement are performed (see section 2.3). Second, we consider a two-steps protocol (later denoted as our 'solution protocol') consisting of (i) a first curing step at 25 °C for 24 h, (ii) demolding, and (iii) a second curing step at 80 °C for 1.5 h. Finally, we consider an alternative two-steps protocol (later denoted as our 'alternative solution protocol') in which the second curing step is performed at 50 °C for 24 h.

2.2. Monitoring of the cross-linking reaction

To monitor the kinetics of solidification of the initially liquid PDMS mixture, we use oscillating shear rheology (AR 2000 rheometer by TA Instrument). We use a plane-conical geometry (cone radius, angle and truncation are 20 mm, 4° and 111 μm, respectively), and measure both the storage and loss moduli of the material, G' and G'' respectively, every 10 s with oscillations of amplitude of 0.5% and a frequency of 1 Hz.

2.3. Measurements on cross-linked samples

For each curing protocol, the elastic penetration depth of a rigid indentor into the cross-linked PDMS is measured on the wafer-like sample molded in the Petri dish, using a commercial Shore A durometer (Shore Instrument & MFG. Co. INC. New York U.S.A.). All measurements are performed following the norm ASTM D2240, and are thus conventionally given as a hardness in shore A units. Note that no irreversible deformation of the material is detected at the indented location. As a consequence, the measurements reflect the elasticity of the sample and not its plasticity, despite the 'hardness' appellation. The measurements are recorded as soon as complete indentation is established, to mitigate against the subsequent relaxation of the elastomer. Each datapoint is the mean value over five measurements, each made at a different location along the sample's surface.

The topography of an about 17 mm × 17 mm central region of the free surface of each parallelepipedic sample is measured using an optical interferometric profilometer (Bruker Contour GT K1), with a (x, y) frame aligned with the sides of the parallelepiped. The topographies are analyzed through the following steps (see figure 3):

- First, by using the Mountains Maps software, a region of interest (ROI) of 14 mm × 14 mm is cropped out of the raw topography (figure 3(a)), with its center matching the center of the mold cavity (identifiable by a slight topography defect due to the milling initiation). Then, the aberrants points(scattered white points in figure 3(a)), inherent to any interferometric techniques, are removed using the tool 'remove outliers'. A central square sub-region (in white in figure 3(a)) is further discarded due to the presence of the above-mentioned milling defect. The topography is then levelled by removing its average plane.
- Second, by using the Matlab software, the levelled topography is fitted with an elliptic paraboloid whose axis of symmetry is parallel to the z-axis, defined by the equation $z = z_0 + \frac{x'^2}{2R_1} + \frac{y'^2}{2R_2}$. z_0 is a non-physical vertical offset, which is then removed from all subsequent steps, thus defining a vanishing height at the apex of the fitted paraboloid.

The iso-heights of the paraboloid are ellipses (see figure 3(b)), the principal axes of which define the in-plane x' and y' axes, that are orthogonal to each other, but rotated by an angle θ with respect to the x and y axes of the acquired topographies (see figure 3(b)). R_1 and R_2 ($R_1 < R_2$) correspond to the radii of curvature of the paraboloid, at its apex, along the x' and y' axes, respectively. An alternative estimator of the flatness error is also computed as the height z_c

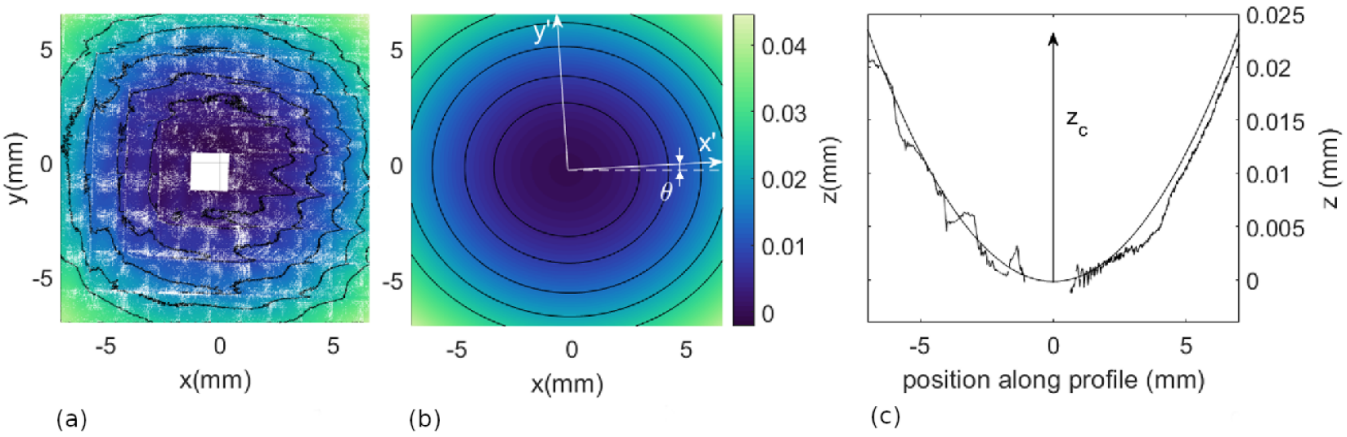

Figure 3. Topography analysis (illustrated on the sample cured with a single-step protocol at 80 °C). (a) Cropped topography, from which the average plane has been removed. Discarded points are in white (aberrant points and central square). Black lines: iso-height curves at $z = 4$, 8, 14, 20 and 26 μm. (b) Fitted paraboloid, with the same iso-height curves (ellipses) as in (a). Definition of the principal axes, x' and y', and their angle θ with respect to the (x, y) frame. (c) Cut across the fitted paraboloid along the x' axis, superimposed with the corresponding cut across the experimental topography. z_c is illustrated.

reached by the fitted paraboloid at an arbitrarily chosen location such that $x' = 7$ mm (corresponding to half of the ROI lateral size) and $y' = 0$ mm. z_c is illustrated on figure 3(c), where a typical experimental topography profile along the x' axis is shown, together with the corresponding profile of the fitted paraboloid. One can see that choosing a paraboloid to fit our experimental data gives reasonably good results, which is confirmed by a large goodness of fit as indicated by R^2 values larger than 0.975 for curing temperatures 50° and 80° (for 25°, the shape error being very small, the signal to noise ratio is weak, thus yielding a much poorer fitting quality). Also note that the paraboloid apex ($x' = y' = 0$ mm in figure 3(b)) is always found close to the center of the ROI ($x = y = 0$ mm in figure 3(b)).

2.4. Finite element calculations

Static finite element simulations of the thermal contraction of our samples are performed using the 'Mechanical' tool within the Ansys software. A parallelepipedic solid of thickness 7.2 mm and a square base of lateral size 21 mm is meshed with rectangular cuboid elements (see figure 7). They possess eight nodes per face and three degrees-of-freedom per node, corresponding to translations in the three directions. Their characteristic size is 0.72 mm (a value that has been checked to be small enough to ensure convergence of the calculations) so that the reference model of figure 7 contains a total of 9000 elements and 40 641 degrees of freedom. The elements are used with homogeneous, isotropic, linear elastic solid behavior. The Poisson's ratio, Young's modulus and coefficient of linear thermal expansion are taken equal to typical values for Sylgard 184 PDMS: respectively 0.49 [36, 37], 1.8 MPa (as measured independently from the relationship between contact area and normal load of a PDMS sphere/glass plane, using Hertz' contact model [38]; method and values similar to [12]) and 3.2×10^{-4} °C^{-1} [37].

3. Results

3.1. Topography results

In this section, we present the results of the topography measurements, performed as described in section 2.3, on the free surface of the samples prepared using the five different curing protocols mentioned at the end of section 2.1. Figure 4(a) shows the x' profiles of the fitted paraboloids, while figure 4(b) represents the evolution of the smallest radius of curvature, R_1, and of the height error estimator, z_c, as a function of the curing protocol. For the single-step protocols, a flatness error is robustly found but it decreases as the curing temperature decreases: z_c is as high as 24 μm ($R_1 \simeq 1$ m) at 80 °C, but drops to values as small as about 3 μm ($R_1 \simeq 7.8$ m) at 25 °C. Note that, for single-step protocols at 50 and 80 °C, R_1 and R_2 are almost equal, indicating a residual shape of the free surface being axi-symmetric around the point $(x' = 0,\ y' = 0)$. In contrast, at 25 °C, we find an anisotropic topography, with $R_2 \simeq 5\, R_1$, i.e. the surface is flatter along the y' axis.

Importantly, we check that the flatness error on the PDMS' free surface does not come from an unwanted shape of either the milled aluminum mold or of the glass lid. To do that, we first measure the topography of the excavated face of the mold, and apply the exact same analysis as for the PDMS surface. We find $R_1 \simeq 8.1$ m and $R_2 \gg R_1$, two features that closely match the results found on the PDMS' free surface after the single step curing at 25 °C. Such a matching strongly suggests that the residual shape found at this temperature is not a replication error, but a faithful replication of a non perfectly flat aluminum mold. This conclusion is further substantiated by our second topography measurement, made on the lid in its clamped position (to account for possible bending effect due to clamping). Indeed, in that case, we find that the topography has a root mean square error of only about 25 nm with respect to a perfect plane, thus excluding any artifact due to the lid.

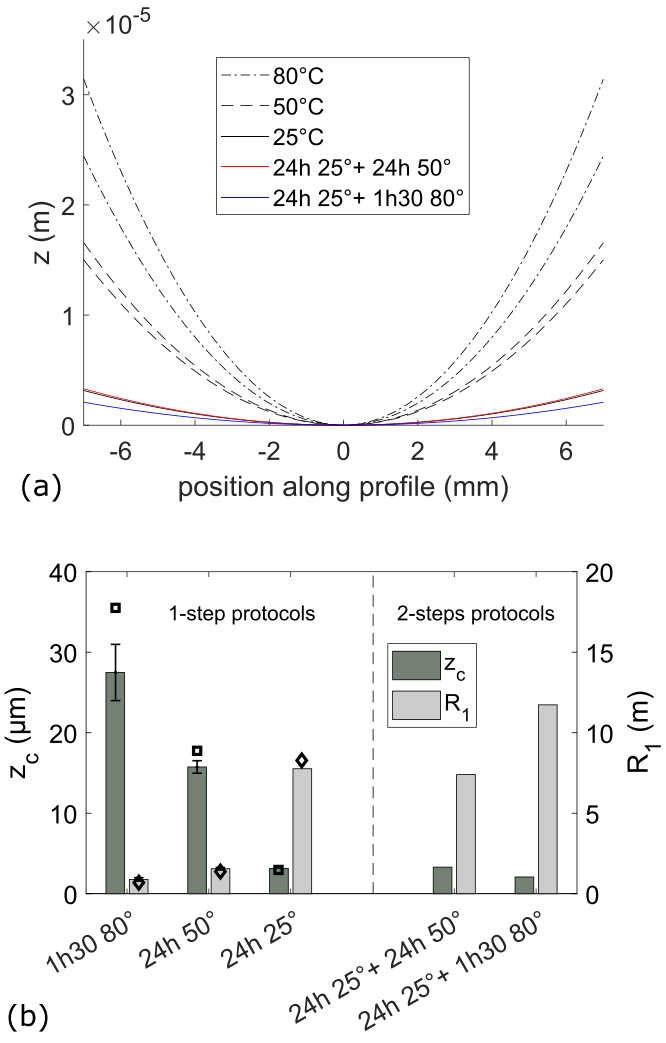

Figure 4. (a) Profiles along x' (showing the smallest radius of curvature, R_1) of the fitted paraboloid of the PDMS's free surface, for the various curing protocols. For each case, z_c is directly readable as the largest height reached on this plot. (b) Evolution of the mean values of R_1 (left axis) and z_c (right axis) as a function of the curing protocol. Error bars are the minimum and maximum observed values. Symbols are the results of the finite element calculations reported in section 3.4.

Crucially, the two two-steps protocols are both found to produce very small residual shapes, characterized by (on the example of our 'solution protocol'): $R_1 \simeq 11.7$ m, $R_2 \simeq 32.1$ m, $z_c \simeq 2.4\,\mu$m (see figure 4). Those values are very similar to that obtained for the single-step protocol at 25 °C.

Importantly for our upcoming discussion, two additional samples prepared using the single-step protocol at 80 °C were found to produce a negligible shape error: (i) a sample with a thickness of 0.72 mm, i.e. ten times smaller than all our other samples ($R_1 \simeq 11.07$ m, $R_2 \simeq 38.53$ m, $z_c \simeq 2.21\,\mu$m) and (ii) a sample with the very same sizes as our reference samples, but peeled off from its glass substrate ($R_1 \simeq 11.04$ m, $R_2 \simeq 36.26$ m, $z_c \simeq 2.22\,\mu$m). Those results will be compared in section 4.4 to dedicated finite elements results described in section 3.4.

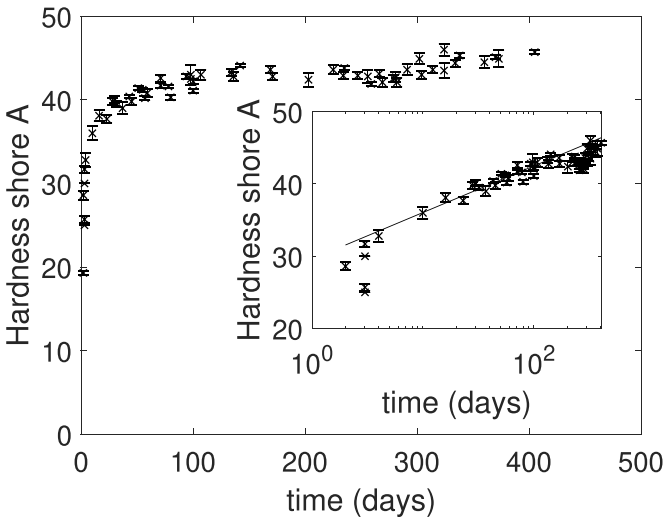

Figure 5. Evolution of the hardness as a function of cross-linking time at 25 °C. Each symbol (error bar) is the mean value (standard deviation) over the five measurements performed on the same sample (see section 2.3). The data include different samples made using different batches. Inset: same data in semi-logarithmic scales. Line: guide for the eye indicating a logarithmic trend.

3.2. Hardness results

We have performed a study of the evolution of the sample hardness (measured as described in section 2.3) as a function of the curing time at 25 °C. The results are shown on figure 5, over a total time longer than a year. As one can see from the alignment of the points in semi-logarithmic scale (inset of figure 5), the hardness increases logarithmically with curing time, until reaching a plateau at 43 ± 2 shore A after about 100 days. In particular, a hardness of only about 25 ± 5 shore A is reached after 48 h at 25 °C, which corresponds to our single-step protocol with the lowest temperature. Note that the hardness plateau, reached while keeping the sample at 25 °C, was found to increase slightly with the temperature of the initial curing phase, e.g. 46.5 ± 1.5 shore A for an initial curing of 5h30 at 50 °C and 49.5 ± 1.5 shore A for an initial curing of 1h30 at 80 °C.

Importantly, the two-steps protocols are found to ensure a final hardness already on a plateau at a value higher than about 43 shore A, indicating a fully completed cross-linking reaction, after a protocol duration of only 26 h ('solution protocol') or 48 h ('alternative solution protocol').

3.3. Rheology results

Figure 6 shows the evolution of G' and G'' (measured as described in section 2.2) as a function of the cross-linking time, for four different cross-linking temperatures: 40, 70, 80 and 100 °C. Note that these results agree quantitatively with those of [39]. The point at which a cross-linking PDMS sample switches from a liquid-dominated behavior to a solid-dominated one is the so-called gel point [40]. The gel point

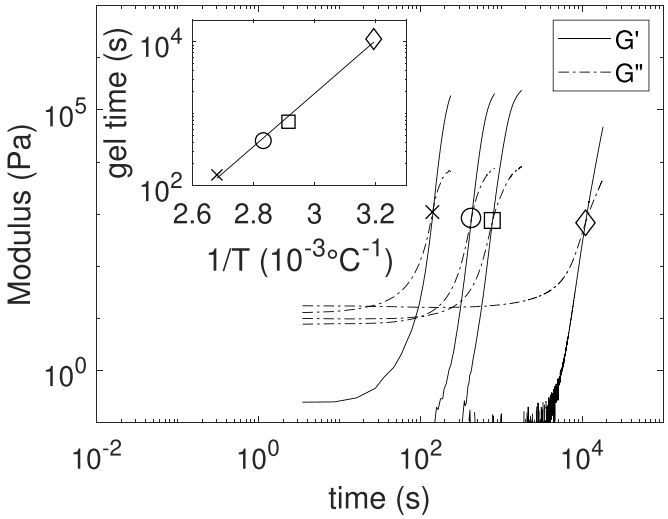

Figure 6. Main: evolution of the viscoelastic moduli, G' and G'', as a function of the cross-linking time, for various curing temperatures (40, 70, 80 and 100 °C, for the curves from right to left), in log–log scales. Symbols: estimated gel points. Inset: estimated gel time as a function of the inverse of the curing temperature, in semi-log scales. Line: exponential fit.

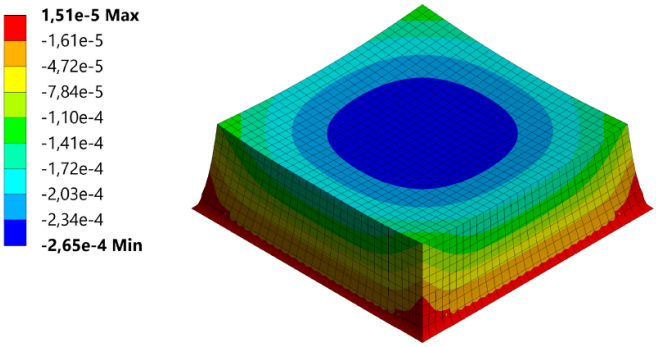

Figure 7. Reference finite element simulation. Cooling of a parallelepipedic PDMS block, stuck to a rigid surface at its bottom boundary, from 80 °C down to 20 °C. The color code indicates vertical displacement, in m, from red (zero displacement at the reference bottom boundary) to blue (maximum downward/negative displacement).

is commonly estimated as the point at which, during cross-linking, G' and G'' become equal [41]. Figure 6 shows that the gel point (symbols) is reached after a shorter time for larger temperatures. Note that the origin of time in this analysis is taken as the instant at which the target temperature is reached in the rheometer, i.e. after about an incompressible 1h30 period dedicated to mixture, degassing, transport to the rheometer and heating ramp to the target temperature.

The inset of figure 6 represents the gel time, GT, as a function of cross-linking temperature. As emphasized by the semi-log representation, the gel time *vs* temperature evolution is well captured by an Arrhenius law (also see [42]) of the type $GT \sim e^{\frac{E_a}{RT}}$, where R is the universal gas constant, T is the absolute cross-linking temperature and E_a is the cross-linking activation energy. Extrapolation of the fitted Arrhenius law (see solid line in inset of figure 6) to 25 °C enables estimating the gel time associated with a cross-linking at 25 °C to about 11 h.

3.4. Finite element results

We perform static finite element calculations (see methods described in section 2.4) aimed at representing the thermal contraction undergone by our samples when cooling from the curing temperature down to the room/operating temperature. A parallelepiped with the same dimensions and material properties as in our experiments is considered. Its faces are all stress-free, except for the bottom face, the nodes of which are fixed in their initial position, to model the fact that, in the experiments, the sample is stuck to its rigid glass plate.

Our reference calculation corresponds to a drop of temperature from 80 °C (the curing temperature) down to 20 °C (a good estimate of the room temperature). As shown in figure 7, the initially perfectly parallelepipedic sample (at 80 °C) ends up having a shape characterized by a concave top surface. Such a feature is in perfect qualitative agreement with our observations of section 3.1. More quantitatively, we fit the concave topography of the top surface of the simulated stuck sample, with the same elliptical paraboloid function used in section 2.3 for our experimental samples. Again, the fitting quality is good ($R^2 = 0.996$) and provides $R_1 = R_2 = 0.68$ m, yielding $z_c \simeq 36\,\mu$m. Similar calculations using an initial temperature of 50 °C (resp. 25 °C) instead of 80 °C led to $R_1 = R_2 = 1.38$ m (resp. $R_1 = R_2 = 8.28$ m) and $z_c \simeq 18\,\mu$m (resp. $z_c \simeq 3\,\mu$m). Those values are in good quantitative agreement with those found experimentally for single-step protocols at the same curing temperatures (see figure 4(b)).

We ran three additional finite element calculations (see figure 8), in which a single feature was varied at a time, compared to the reference calculation of figure 7. In the first one, we test a potential influence of the overall sample size, while the last two calculations are meant to simulate the thermal contraction expected in the two additional experiments described at the end of section 3.1.

Figure 8(a) presents the results of a simulation in which all sizes of the sample are divided by a factor of 10^5, so that the sample's lateral size is reduced to 210 nm. We can see that the exact same geometrical shape is recovered, with vertical displacements of the top free surface being 10^5 times smaller than in the reference simulation of figure 7.

Figure 8(b) presents the results of a simulation in which the sample thickness has been divided by 10, while the lateral sizes are kept unchanged. The final shape is now very different from the reference case of figure 7. The top free surface is now essentially flat over a large central region, while deviations from flatness are localized around the periphery of the sample.

Figure 8(c) presents the results of our last calculation, with the same geometry as the reference one except that the bottom face is also stress-free. As can be seen, the sample keeps its perfect parallelepipedic shape, and only shrinks isotropically.

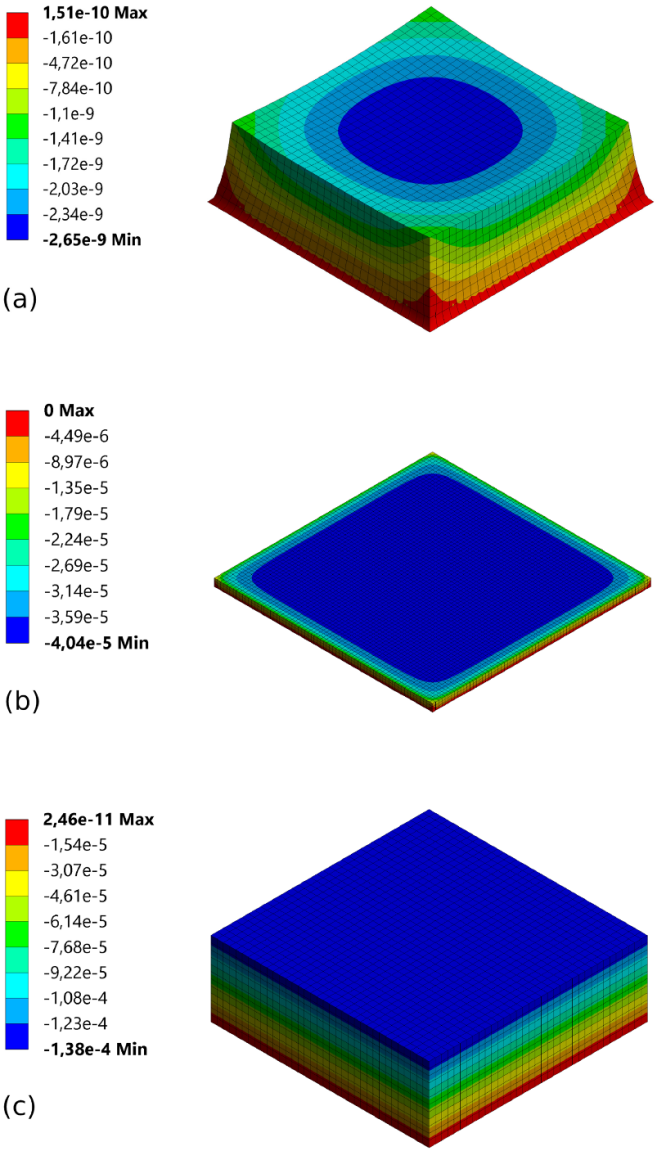

Figure 8. Additional finite element simulations, represented in the same way as in figure 7. (a) Same as reference simulation of figure 7, but for a sample with all dimensions and mesh size divided by a factor of 10^5. (b) Same as reference simulation, but for a sample with a thickness divided by a factor of 10. The volume is meshed with rectangular cuboid elements of characteristic size 300 μm. (c) Same volume and mesh as reference simulation, but when all faces are stress-free.

4. Discussion

4.1. Replication shape errors can be avoided with a two-steps curing protocol

As we have seen in section 3.1, samples prepared with a single-step curing protocol suffer from a systematic shape error, which increases with the curing temperature (see figure 4) and only vanishes when the curing temperature is sufficiently close to the final operating temperature (in our case the room temperature, about 20 °C). Our results of section 3.2 have also shown that, when curing is performed close to the room temperature, the curing time necessary to fully complete the cross-linking reaction is about 100 days (see figure 5). Such a duration is a very inconvenient time for sample preparation, much longer than any time used in the protocols from the literature. In this context, we conclude that there is no single-step curing protocol that both avoids replication errors and reaches full cross-linking within a reasonable time (say at most a couple of days).

In contrast, our two-steps 'solution protocol' (resp. 'alternative solution protocol') does enable simultaneously a negligible shape error (see figure 4) and a fully completed cross-linking (the hardness has already reached the 43 shore A plateau visible in figure 5), within less than 26 h (resp. 48 h). We thus recommend to use our 'solution protocol' (described in the end of section 2.1) whenever a faithful molding is required with PDMS Sylgard 184. Note that our solution protocol is in line with the study of Wong [43], who proposed a two-steps protocol to avoid global curvature of PDMS sample cured in a temperature gradient.

4.2. Discussion of the solution protocol

The rationale behind our two-steps 'solution protocol' is the following, and is similar to that discussed in [43]. As seen in section 3.1, to avoid/minimize replication errors, one needs to start curing the sample at the temperature at which it will be subsequently used. This is why the first step is a curing step at 25 °C. The duration of this first step needs to be as short as possible, for the sake of sample production logistics, but long enough for the sample to reach a stable macroscopic shape. The latter requirement amounts to pass the gel time, which marks the transition to a solid state of the sample. As estimated in section 3.3, at 25 °C, the gel time is about 11 h, i.e. shorter than the 24 h of the first curing step of our 'solution protocol', strongly suggesting that the PDMS sample is already solidified at the end of this first step. This is confirmed by the fact that demolding is fully possible at that stage. This conservative value of 24 h has proved to ensure safe replication in various atmospheric conditions, and irrespective of the PDMS batch.

The role of the second curing step at a higher temperature of 80 °C is then to complete the cross-linking reaction within a much shorter time than the 100 days that would be necessary at 25 °C (see figure 5). This acceleration of the reaction is found to be efficient, without generating any additional replication error. Completion of the cross-linking reaction is indicated by a hardness very close to the plateau value (43 shore A) while, after the first curing step, it is still smaller than 25 shore A (the value after 48 h at 25 °C, already mentioned in section 3.2).

It is interesting to note that the moment at which demolding is performed is also important. Indeed, for a second curing step of 24 h at 50 °C, when demolding only after the second curing step, we find replication errors $z_c \simeq 6.0$ μm, larger than what is found when demolding between the two curing steps ($z_c \simeq 3.1$ μm). We currently lack an explanation for this observation.

4.3. Origin of replication errors: thermal contraction

As we have seen, the observed replication errors are directly related to the curing temperature used to reach the gel time; in

addition, those errors vanish when the curing temperature is equal to the final operating temperature of the PDMS sample. In this context, we hypothesize that the observed shape errors are related to the thermal contraction occurring when cooling the sample, from the temperature at which it reached the gel point down to room temperature. Note that the former temperature is the curing temperature for single-step protocols, but is 25 °C (the temperature of the first curing step) for our two-steps protocols. The finite element results of section 2.4 strongly suggest that this hypothesis is valid. Indeed, as shown in figure 4(b), the finite element results provide a good global quantitative agreement with the measurements of R_1 and z_c obtained for the single-step protocols. Consistently with our hypothesis, for the two-steps protocols, the shape errors are almost equal to those of the 25 °C single-step protocol.

Based on this extensive quantitative agreement between experiments and simulations, we can thus conclude that boundary-frustrated thermal contraction (the single ingredient accounted for in our finite element calculations) is the dominant phenomenon responsible for the replication errors observed with single-step protocols at a curing temperature higher than the final operating temperature of the sample. Note that we cannot exclude the possibility that another sample contraction occurs in our experiments, which would be associated with the cross-linking reaction and polymer-network formation rather with the sample's cooling phase. But if present, such an effect must be much smaller than that of the post-gel-point thermal contraction, because the latter already quantitatively captures most of the observations without any adjustable parameter. In addition, we expect that such a curing-originated contraction would occur systematically, irrespective of the details of the curing protocol, which would not explain why the observed shape error is strongly curing-temperature-dependent, nor why it vanishes with our two-steps protocols.

4.4. General implications on replication shape errors

Let us now discuss the implications of thermal contraction being the physical origin of the observed replication shape errors. The first implication is that the effect is expected to be active not only at the centimetric scale of our experiments, but also at any length scale including, e.g. nanometric scales. Indeed, as illustrated in figure 8(a), for any homothetic skrinking of the system considered in the reference calculation of figure 7, the final geometrical shape will be exactly the same, in the sense that all sizes in all directions will be scaled down by the same factor. Thus, replication errors due to thermal contraction are generically expected, irrespective of the length scale of the sample, down to the nanoscales.

The second implication is that a change in the aspect ratio of the sample will affect the shape error. As one can see in figure 8(b), where the sample thickness has been divided by 10 without changing the horizontal dimensions, the final shape is now very different from the reference case of figure 7. The top free surface is now essentially flat over a large central region, a feature which is in perfect agreement with the negligible shape error measured experimentally in the central part of the free surface of a sample with the same dimensions (see end of section 3.1). Deviations from flatness are localized around the periphery of the sample. Such a shape indicates that the flatness error on a parallelepipedic sample is an edge effect, affecting the top surface topography only over a lateral size of order the sample's thickness. In this context, we speculate that the fact that replicated surface textures (including those at nanoscale) often have much smaller out-of-plane sizes than their in-plane dimensions [24, 44, 45] is a potential explanation of why replication shape errors have mainly remained unnoticed.

The third implication is that the final shape observed in figure 7 is fundamentally related to the fact that the PDMS is stuck to the rigid glass plate (represented by fixed nodes at the bottom face in the reference finite element calculations): at the PDMS/glass interface, no displacement is allowed, which impedes the homothetic size-change of the sample that would occur if the sample was free of any boundary constraint (as seen e.g. in [21]). And indeed, both the additional finite element calculation with free nodes at the bottom face (see figure 8(c)) and the topography measurements performed on a sample that was peeled off from its glass substrate (see end of section 3.1) do indicate an absence of shape error in those fully stress-free boundary conditions. Given that many PDMS samples are completely removed from their mold before subsequent use, thermal contraction will mainly cause a global size error, but with presumably little shape error, which provides another potential explanation of why shape errors during replication are not systematically observable.

4.5. Further comments

Note that sample shrinkage associated with PDMS curing at higher-than-room-temperature had previously been investigated in relation with replication. For instance, for fully demolded samples, it was shown to be responsible for too small sample dimensions, by up to a few percents, an effect possibly compensated by using a mold adequately larger than the final desired size [21, 45]. The same effect was also found responsible for debonding between PDMS and a copper electrode in neural prosthesis applications [46] or for a global curvature in fully demolded samples cured in a temperature gradient on a hot plate [43]. We emphasize that, here, we showed that the effect is also relevant for samples submitted to a homogeneous curing temperature (in an oven), and which are not fully demolded but remain perfectly stuck on a rigid substrate. Finally, in other contexts, the same thermal effect, which is a problem for replication, has instead been taken advantage of to measure the Poisson ratio and coefficient of thermal expansion of PDMS Sylgard 184 [37].

Eventually, also note that we observed an additional evolution of the sample shape over very long timescales (typically months), characterized by an increase of z_c (by typical amounts of a few μm) and a reduction of the anisotropy of the flatness error, when any. Such aging of the samples occurs at constant, room temperature, and is thus of a different physical

origin from that relevant during the initial curing protocol. Explaining the origin of such aging is beyond the scope of the present work, but may constitute an interesting topic for future studies.

5. Conclusion

In this work, we questioned the replication quality of samples with a nominally flat surface using PDMS Sylgard 184. We first showed that most of the single-step curing protocols used in the literature yield flatness errors of typical order tens of micrometers out-of-plane over 1 cm along the plane (section 3.1). Such errors are expected to be generally problematic, in particular for all applications in which the surface needs to be brought into contact with another flat solid, like in tribology [17] or in microfluidics [47].

We showed that this effect arises when the thermal contraction of the PDMS sample, when cooling from the temperature at which it reached the gel point down to its final operating temperature, is frustrated by some mechanical constraint (sections 4.3 and 4.4). In our case, frustration was due to the fact that the sample was molded directly on its final rigid substrate (a glass plate). As a counter-measure, we have identified a two-steps curing protocol (the 'solution protocol' described in the end of section 2.1) that enables faithful mold replication. Its main features are first to reach the gel point of the PDMS through an initial curing step at the final operating temperature, and then to complete cross-linking within a reasonable time through a higher-temperature second curing step.

Our 'solution protocol' will be useful in any situation in which a good control of the sample's shape is required. Identifying thermal contraction as the physical origin of the identified replication error implies that those errors are expected at any length scale, and that they strongly depend on the sample's aspect ratio and boundary conditions. Although our results have been obtained on parallelepipedic samples, we expect that the insights brought will be useful to develop mitigation strategies against replication errors that will be suitable in any other sample geometry.

Conversely, the insights we provided about the physical origin of the final shape of replicated PDMS samples may open the way to the production of desired deviations to flatness, tunable through the curing protocol. For instance, one could prepare curved micro-fluidic channels that may be useful in cell trapping [48] or molds for microlenses useful for instance for robot vision [31].

Data availability statement

All data that support the findings of this study are included within the article.

Acknowledgment

This work has been funded by the French ANR, through Grant ANR-18-CE08-0011-01 (PROMETAF project).

ORCID iDs

Emilie Delplanque https://orcid.org/0000-0003-2843-2481
Antoine Aymard https://orcid.org/0000-0002-1825-8152
Davy Dalmas https://orcid.org/0000-0001-6010-8804
Julien Scheibert https://orcid.org/0000-0002-9600-3796

References

[1] Menard E and Rogers J A 2010 Springer handbook of nanotechnology *Stamping Techniques for Micro- and Nanofabrication* ed B Bhushan (Berlin: Springer) pp 313–32
[2] Con C and Cui B 2013 Effect of mold treatment by solvent on PDMS molding into nanoholes *Nanoscale Res. Lett.* **8** 394
[3] Persson J S, Tiwari A, Valbahs E, Tolpekina T V and Persson B N J 2018 On the use of silicon rubber replica for surface topography studies *Tribol. Lett.* **66** 140
[4] Pérez-Calixto D, Zamarrón-Hernández D, Cruz-Ramírez A, Hautefeuille M, Hérnandez-Cordero J, Velázquez V and Grether M 2017 Fabrication of large all-PDMS micropatterned waveguides for lab on chip integration using a rapid prototyping technique *Opt. Mater. Express* **7** 1343–50
[5] Chai H, Chen F, Song Z, Xiong L, Xiao G, Lu Z and Yu L 2021 A versatile wax assisted double replica molding and its application in flexible electronic skin *Sens. Actuator* B **343** 130132
[6] McDonald J C and Whitesides G M 2002 Poly(dimethylsiloxane) as a material for fabricating microfluidic devices *Acc. Chem. Res.* **35** 491–9
[7] Raj M K and Chakraborty S 2020 PDMS microfluidics: a mini review *J. Appl. Polym. Sci.* **137** 48958
[8] Scheibert J, Leurent S, Prevost A and Debrégeas G 2009 The role of fingerprints in the coding of tactile information probed with a biomimetic sensor *Science* **323** 1503–6
[9] Whitesides G M and Robotics S 2018 *Angew. Chem., Int. Ed.* **57** 4258–73
[10] Tao H and Gibert J 2020 Multifunctional mechanical metamaterials with embedded triboelectric nanogenerators *Adv. Funct. Mater.* **30** 2001720
[11] Prevost A, Scheibert J and Debrégeas G 2013 Probing the micromechanics of a multi-contact interface at the onset of frictional sliding *Eur. Phys. J.* E **36** 17
[12] Sahli R, Pallares G, Ducottet C, Ben Ali I E, Al Akhrass S, Guibert M and Scheibert J 2018 Evolution of real contact area under shear and the value of static friction of soft materials *Proc. Natl Acad. Sci. USA* **115** 471–176
[13] Acito V, Ciavarella M, Prevost A M and Chateauminois A 2019 Adhesive contact of model randomly rough rubber surfaces *Tribol. Lett.* **67** 54
[14] Tinnemann V, Hernández L, Fischer S C L, Arzt E, Bennewitz R and Hensel R 2019 In situ observation reveals local detachment mechanisms and suction effects in micropatterned adhesives *Adv. Funct. Mater.* **29** 1807713
[15] Vakis A I *et al* 2018 Modeling and simulation in tribology across scales: an overview *Tribol. Int.* **125** 169–99
[16] Schmid H and Michel B 2000 Siloxane polymers for high-resolution, high-accuracy soft lithography *Macromolecules* **33** 3042–9
[17] Romero V, Wandersman E, Debrégeas G and Prevost A 2014 Probing locally the onset of slippage at a model multicontact interface *Phys. Rev. Lett.* **112** 094301

[18] O'Neill A, Soo Hoo J, and Walker G Rapid curing of PDMS for microfluidic applications *Chips Tips* (available at: https://blogs.rsc.org/chipsandtips/2006/10/23/rapid-curing-of-pdms-for-microfluidic-applications/?doing_wp_cron=1645882052.6609981060028076171875)
[19] Oyama T G, Oyama K and Taguchi M 2020 A simple method for production of hydrophilic, rigid and sterilized multi-layer 3D integrated polydimethylsiloxane microfluidic chips *Lab Chip* **20** 2354–63
[20] Shin Y S, Cho K, Lim S H, Chung S, Park S-J, Chung C, Han D-C and Chang J K 2003 PDMS-based micro PCR chip with Parylene coating *J. Micromech. Microeng.* **13** 768–74
[21] Lee S W and Lee S S 2008 Shrinkage ratio of PDMS and its alignment method for the wafer level process *Microsyst. Technol.* **14** 205–8
[22] Jo B-H, Van Lerberghe L M, Motsegood K M and Beebe D J 2000 Three-dimensional micro-channel fabrication in polydimethylsiloxane (PDMS) elastomer *J. Microelectromech. Syst.* **9** 76–81
[23] Klemic K G, Klemic J F and Sigworth F J 2005 An air-molding technique for fabricating PDMS planar patch-clamp electrodes *Pflügers Arch.* **449** 564–72
[24] Cherng Y-S and Su G-D J 2014 Fabrication of polydimethylsiloxane microlens array on spherical surface using multi-replication process *J. Micromech. Microeng.* **24** 015016
[25] Nase J, Lindner A and Creton C 2008 Pattern formation during deformation of a confined viscoelastic layer: from a viscous liquid to a soft elastic solid *Phys. Rev. Lett.* **101** 074503
[26] Barreau V, Hensel R, Guimard N K, Ghatak A, McMeeking R M and Arzt E 2016 Fibrillar elastomeric micropatterns create tunable adhesion even to rough surfaces *Adv. Funct. Mater.* **26** 4687–94
[27] Wu C Y, Chiang T H and Hsu C C 2008 Fabrication of microlens array diffuser films with controllable haze distribution by combination of breath figures and replica molding methods *Opt. Express* **16** 19978–86
[28] Vozzi G, Flaim C J, Bianchi F, Ahluwalia A and Bhatia S 2002 Microfabricated PLGA scaffolds: a comparative study for application to tissue engineering *Mater. Sci. Eng.* C **20** 43–7
[29] Liu H-B and Gong H-Q 2009 Templateless prototyping of polydimethylsiloxane microfluidic structures using a pulsed CO_2 laser *J. Micromech. Microeng.* **19** 037002
[30] Gombert Y, Simič R, Roncoroni F, Dübner M, Geue T and Spencer N D 2019 Structuring hydrogel surfaces for tribology *Adv. Mater. Interf.* **6** 1901320
[31] Zhu X, Chen H, Zhu L, Wang H and Zhang W 2014 Fabrication of curved microlens array using a drop-on-demand droplet generator and polydimethylsiloxane replica mold *Opt. Eng.* **53** 1–9
[32] Kumar A, Biebuyck H A and Whitesides G M 1994 Patterning self-assembled monolayers: applications in materials science *Langmuir* **10** 1498–1511
[33] Rosenthal A, Macdonald A and Voldman J 2007 Cell patterning chip for controlling the stem cell microenvironment *Biomaterials* **28** 3208–16
[34] Scheibert J, Prevost A, Debrégeas G, Katzav E and Adda-Bedia M 2009 Stress field at a sliding frictional contact: experiments and calculations *J. Mech. Phys. Solids* **57** 1921–33
[35] SYLGARD^{TM} 184 Silicone Elastomer Kit Technical Data Sheet (available at: www.dow.com/en-us/document-viewer.html?ramdomVar=6028251085099047358&docPath=/content/dam/dcc/documents/en-us/productdatasheet/11/11-31/11-3184-sylgard-184-elastomer.pdf) (Accessed 1 July 2021)
[36] Lengiewicz J, de Souza M, Lahmar M A, Courbon C, Dalmas D, Stupkiewicz S and Scheibert J 2020 Finite deformations govern the anisotropic shear-induced area reduction of soft elastic contacts *J. Mech. Phys. Solids* **143** 104056
[37] Müller A, Wapler M C and Wallrabe U 2019 A quick and accurate method to determine the Poisson's ratio and the coefficient of thermal expansion of PDMS *Soft Matter* **15** 779–84
[38] Popov V L 2017 *Contact Mechanics and Friction* (Berlin: Springer)
[39] Giustiniani A 2017 Linking adhesive properties and pore organisation of silicone emulsions obtained by reactive blending *PhD Thesis* Université Paris Saclay
[40] Winter H H 2016 Gel point Gel Point. In Encyclopedia of Polymer Science and Technology (Hoboken, NJ: John Wiley) pp 1–15
[41] Tung C-Y M and Dynes P J 1982 Relationship between viscoelastic properties and gelation in thermosetting systems *J. Appl. Polym. Sci.* **27** 569–74
[42] Payet L, Ponton A, Agnely F, Colinart P and Grossiord J L 2002 Caractérisation rhéologique de la gélification d'alginate et de chitosane: effet de la température *Rhéologie* **2** 46–51 (available at: http://www.legfr.fr/IMG/pdf/Revue/Vol2/Payet_Vol.2_pp46-51_2002.pdf)
[43] Wong E J 2010 Modeling and control of rapid cure in polydimethylsiloxane (PDMS) for microfluidic device applications *PhD Thesis* Massachusetts Institute of Technology
[44] Tong J, Simmons C A and Sun Y 2008 Precision patterning of PDMS membranes and applications *J. Micromech. Microeng.* **18** 037004
[45] Madsen M H, Feidenhans'l N A, Hansen P-E, Garnæs J and Dirscherl K 2014 Accounting for PDMS shrinkage when replicating structures *J. Micromech. Microeng.* **24** 127002
[46] Mao Y, Pechenizkiy I, Stieglitz T and Doll T 2021 Numerical evaluation on residual thermal stress-induced delamination at PDMS–Metal interface of neural prostheses *Micromachines* **12** 669
[47] Abidin U, Daud N A S M and Le Brun V 2019 Replication and leakage test of polydimethylsiloxane (PDMS) microfluidics channel *AIP Conf. Proc.* **2062** 020064
[48] Abdelgawad M, Wu C, Chien W-Y, Geddie W R, Jewett M A S and Sun Y 2011 A fast and simple method to fabricate circular microchannels in polydimethylsiloxane (PDMS) *Lab Chip* **11** 545–51